Journal of Materials Chemistry C

meso-Ethynyl-extended push-pull type porphyrins for near-infrared organic photodetectors

Journal:	*Journal of Materials Chemistry C*
Manuscript ID	TC-ART-02-2022-000588.R1
Article Type:	Paper
Date Submitted by the Author:	12-Jun-2022
Complete List of Authors:	Gielen, Sam; Hasselt University Faculty of Sciences, Chemistry Cuesta Gomez, Virginia; University de Castilla-la Mancha, Institute for Nanoscience and Molecular Materials Brebels, Sonny; Universiteit Hasselt Faculteit Wetenschappen, IMO/IMOMEC Quill, Tyler; Stanford University Vanderspikken, Jochen; Hasselt University Faculty of Sciences, Lutsen, Laurence; IMEC de la Cruz, Pilar; Universidad Castilla La Mancha, Institute of Nanoscience, Nanotechnology and Materials Science Vandewal, Koen; Universiteit Hasselt Faculteit Wetenschappen, IMO/IMOMEC Langa, Fernando; University de Castilla-la Mancha, Institute for Nanoscience and Molecular Materials Maes, Wouter; Hasselt University Faculty of Sciences, Chemistry

meso-Ethynyl-extended push-pull type porphyrins for near-infrared organic photodetectors

Sam Gielen[a,b,c], Virginia Cuesta Gómez[d], Sonny Brebels[a,b,c], Tyler James Quill[e], Jochen Vanderspikken[a,b,c,e], Laurence Lutsen[b,c], Pilar de la Cruz[d], Koen Vandewal[a,b,c], Fernando Langa[d], Wouter Maes[a,b,c]*

[a] UHasselt – Hasselt University, Institute for Materials Research (IMO), Agoralaan 1 – Building D, 3590 Diepenbeek, Belgium
E-mail: wouter.maes@uhasselt.be

[b] IMEC, Associated Lab IMOMEC, Wetenschapspark 1, 3590 Diepenbeek, Belgium

[c] Energyville, Thorpark, 3600 Genk, Belgium

[d] Universidad de Castilla-La Mancha, Institute of Nanoscience, Nanotechnology and Molecular Materials (INAMOL), Campus de la Fábrica de Armas, Toledo, Spain

[e] Stanford University, Department of Materials Science and Engineering, Stanford, CA 94305, USA

Abstract

Natural porphyrins play a key role in a range of vital functions such as oxygen transport in the bloodstream and the conversion of light to chemical energy in plants. Likewise, synthetic porphyrin derivatives can be used to detect light and convert it into an electrical current in photodiodes. The versatility of porphyrinoid chemistry allows to extend the absorptivity (and hence detectivity) to the near-infrared while maintaining good solubility, suitable electrochemical properties, and compatibility with the electron acceptor molecules required to achieve a reasonable photocurrent. Here, our efforts on the design and synthesis of novel push-pull type *meso*-ethynyl-extended porphyrin compounds, both of A-D-A and D-A-D type (D = donor, A = acceptor), and their evaluation in prototype near-infrared organic photodetector devices are presented. The push-pull design with strongly electron-deficient building blocks results in absorption onsets up to 1200 nm, translating in an optical gap approaching 1 eV. Both A-D-A and D-A-D small molecules show good photodetector performance, with a peak specific detectivity near $2x10^{11}$ and $4x10^{11}$ Jones at 1000 nm (at -2 V bias), respectively. These values are among the best reported so far for small molecule based near-infrared organic photodetectors.

Introduction

Modern applications are often nature-inspired, in the sense that we humans try to mimic a specific strategy adopted by nature.[1] An example is the 'lotus effect', referring to the self-cleaning properties of a surface as a result of the ultra-hydrophobicity as observed on lotus leaves.[2] The human sight presents another interesting example, for which we have invented the camera.[3] The sensitivity of our eyes is truly impressive and finds its origin in a sequence of complex chemical and physical processes. The chromophore interacting with (visible) light is retinal. Upon photon absorption, the configuration of the retinal molecule is altered from the curved *cis* isomer to the straight *trans* isomer. This configurational change triggers a chemical cascade in the neighboring opsin protein that results in the perception of light or images in our brain.[4] Although the result is the same for man-made cameras (i.e. an image), the principle of capturing light and converting it into an image is fundamentally different. Whereas *cis-trans* isomerization occurs in retinal upon light absorption, man-made devices make use of semiconductors that generate free charges upon photon absorption (the 'photovoltaic effect'). It has some similarities with the photoconversion process in green plants converting sunlight, via a series of electron transfer events, into a chemical potential and stored chemical energy. The active organic materials used in plants are chlorophyll molecules, which are porphyrin derivatives.[5] Therefore, it feels 'natural' to use porphyrin molecules as active materials for photovoltaic and photo-sensing applications as well.

Substituted porphyrin molecules are categorized as 'small molecule' chromophores. Compared to (conjugated) polymers, their size and molar mass is well defined, without notable batch-to-batch or end group variations.[6, 7] This makes small molecules more attractive in terms of reproducible physicochemical and optoelectronic properties. Additionally, the conjugation length is strictly defined, resulting in more narrow absorption bands.[8] Consequently, the absorption edge is sharper and with that the energy loss in the photovoltaic process is reduced. On the other hand, the conjugated system is smaller as compared to polymers, which limits the optical gap. Nevertheless, reducing the bond-length alternation, enforcing molecular planarity, increasing the aromatic resonance energy or using the 'strong donor-strong acceptor' concept does allow to red-shift the absorption of molecular chromophores to a certain extent.[9] Nowadays, small organic molecules with an optical gap as low as 0.17 eV are known.[10] Nonetheless, the majority of near-infrared (NIR) photoactive organic semiconductors reported to date are polymer-based. In particular, the research performed on small molecule chromophores in the field of NIR organic photodetectors (OPDs) is limited to a handful of examples. In most cases, phthalocyanine or porphyrin derivatives have been used, but examples with squaraine, boron dipyrromethene (BODIPY), and indacenedithiophene-benzothiadiazole-rhodanine (IDTBR) have been reported as well.[11] Quite often, NIR detectivity is claimed, but significant NIR absorption (above 900 nm) is only observed as tail absorption. In this respect, studies worth mentioning are the ones presented by M. Young *et al.*,[12] Z. Su *et al.*,[13] and J. Zimmerman *et al.*,[14] who used an organic heptamethine salt (in combination with C_{60}), lead phthalocyanine (PbPc, with C_{70}), or a porphyrin tape (with C_{60}), respectively. The organic heptamethine (tetrafluoroborate) salt allowed to detect wavelengths as long as 1500 nm with a peak external quantum efficiency (EQE) of 2% at 1300 nm.[12] The PbPc:C_{70} combination afforded a higher peak efficiency of 30% but only at 900 nm,[13] while the porphyrin tape generated 6.5% EQE at 1350 nm.[14] Therefore, it seems justified to state that NIR-photoactive small molecules are currently underexplored compared to polymeric variants.[11, 15-17]
In this work, we investigate nature-inspired porphyrinoid semiconductors for their use in NIR OPDs. Red-shifting the absorption spectrum is enabled by the multiple chemical modifications possible on the porphyrin scaffold. The β- and *meso*-positions can be varied and the porphyrinato ligand can be metalated, allowing a large structural degree of freedom to tune the porphyrinoid chromophore.[18, 19] An interesting class of porphyrinoid materials, the *meso*-ethynyl-bridged acceptor-donor-acceptor (A-D-A) and donor-acceptor-donor (D-A-D) type porphyrins, with the porphyrin as the D part, allows the combination with electron acceptors of various strength to obtain a more red-shifted absorption.[20, 21] So far, only one monomeric *meso*-ethynyl-extended A-D-A porphyrinoid material has been applied as

a NIR OPD active material. In this report by L. Li *et al*., the A part was a benzothiadiazole, which is known to have a modest acceptor strength, yielding an absorption onset of 950 nm.[22]

Here, the porphyrin (Por) donor part is combined with multiple acceptors of various strength in an A-D-A or D-A-D configuration. Combination with thieno[3,4-*b*]pyrazine (TP), thiadiazolo[3,4-*g*]quinoxaline (TQ), and benzobisthiadiazole (BBT) acceptors resulted in peak absorptions near 800, 950, and 1000 nm, respectively, for the A-D-A type molecules. In the case of the D-A-D materials, two different TQ moieties were combined with the porphyrin donor, yielding peak absorptions near 900 and 1000 nm. The **TQ-Por-TQ** and **Por-TQ-Por** molecules were blended with $PC_{71}BM$ and tested in OPD devices. Optimization of the solvent system, additive concentration, and solvent vapor annealing resulted in a maximum specific detectivity (D^*) of 4 x 10^{11} Jones (at -2 V bias) at 1000 nm.

Results and discussion

The vast number of possibilities to modify the porphyrin scaffold allows to fine-tune the final material properties in terms of solubility, spectral response, energy levels, and charge carrier mobility. In this work, only the four *meso*-positions have been substituted, of which two (for A-D-A) or three (for D-A-D) positions were used for attaching small alkylated aromatic moieties, primarily to increase the solubility according to the length and branching of the alkyl chains (Scheme 1). Besides, the small aromatic rings somewhat extend the chromophore (despite the torsion angles) and with that a slightly red-shifted absorption is realized. The remaining *meso*-positions were used to link acceptor units with increasing strength, with the intention to shift the absorption spectrum into the NIR. The attachment of the acceptor units to the porphyrin core was done using ethynyl linkers to keep the molecular chromophores planar and therefor efficiently extend the conjugated system. Finally, it was opted to introduce Zn(+II) as metal ion since solvent coordination to the Zn center has previously been shown to be advantageous for solution processing.[18]

The porphyrin materials targeted in this study are ethynyl-bridged *trans*-A_2B_2- and A_3B-Zn(II)-porphyrins (Scheme 1). For the *trans*-A_2B_2-porphyrins, multiple synthetic routes are known to build the porphyrin core. The synthetic route chosen here is outlined in Scheme S1, affording the 5,15-bis(ethynyl)porphyrin precursor **9**.[23] Likewise, the mono-alkynated A_3B-porphyrin precursor **12** was synthesized starting from pyrrole, 5-hexylthieno[3,2-*b*]thiophene-2-carbaldehyde, and trimethylsilylcarbaldehyde, as shown in Scheme S2.[24] Upon Sonogashira cross-coupling with suitable acceptor moieties, these porphyrin cores should give access to the envisaged push-pull structures (Scheme 1, strategy 1).

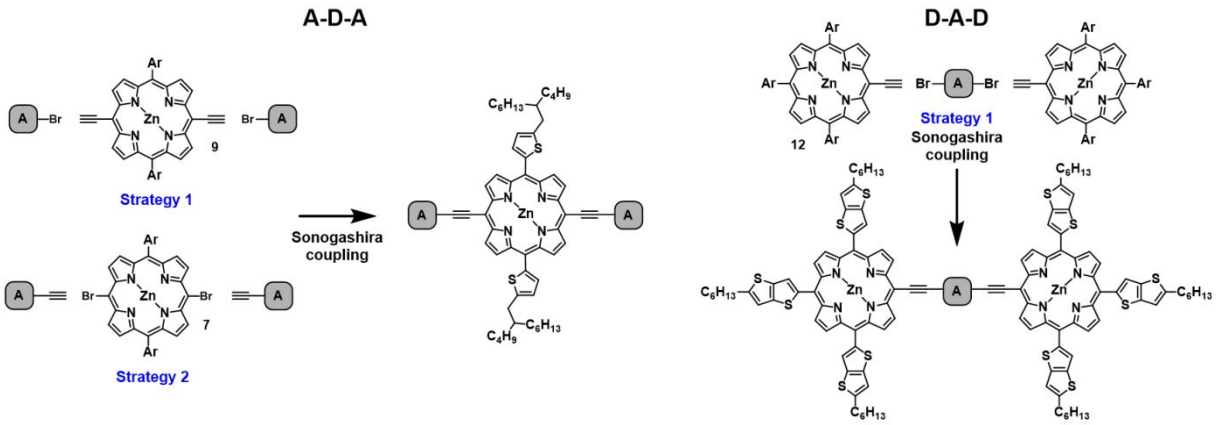

Scheme 1: *A_2B_2- and A_3B-Zn(II)-porphyrin precursors required for the final Sonogashira cross-couplings to yield the envisioned A-D-A and D-A-D type end products. The alkyne moiety can be either on the porphyrin donor (strategy 1) or on the acceptor building block (strategy 2).*

The final Sonogashira cross-coupling between the porphyrin donor and the acceptors is also possible with the alkyne moiety positioned on the acceptor components (Scheme 1, strategy 2). It was shown

before that this procedure reduces the amount of homocoupling (affording A-D-D-A type side products).[25] Therefore, this synthesis route was initially followed for the A-D-A type porphyrins with the aim to increase the yield of the desired product and to simplify purification. Different acceptor moieties of varying 'pull' character were considered and their synthesis was attempted (see Section 3 in the Supporting Information, SI). Unfortunately, it turned out that the acceptor building blocks were either quite insoluble or cleavage of the trimethylsilyl protective group gave rather unstable products that degraded during the reaction and/or purification. To produce the intended porphyrin materials, the Sonogashira cross-coupling was attempted directly after the deprotection for one of the alkynated acceptor molecules (thienoisoindigo (TII) **29**), without prior purification. From ^{1}H-NMR analysis, the deprotected TII-alkyne acceptor **32** was assessed to be relatively pure (Figure S31) and was hence coupled to the dibrominated porphyrin core **7** (Scheme S10). Investigation of the crude reaction product after the Sonogashira reaction via matrix-assisted laser desorption-ionization - time of flight (MALDI-ToF) mass spectrometry (Figure S32) confirmed the formation of the intended A-D-A molecule, as well as multiple undesired (homocoupled) compounds. Sonogashira cross-coupling via this route thus still resulted in an entire range of products and a very low yield (< 10%) of the desired A-D-A compound. For this reason, this strategy was abandoned and we redirected our attention to the synthesis protocol starting from the *meso*-ethynyl-substituted A_2B_2- and A_3B-porphyrins **9** and **12** (strategy 1 in Scheme 1).

For this approach, four different monobrominated and two different dibrominated acceptor building blocks were synthesized (see Scheme S3 and S4), as required for the A-D-A and D-A-D type porphyrins, respectively (Scheme 1). From the building blocks used in the 'failed' strategy 2, thiadiazolo[3,4-*g*]quinoxaline, thieno[3,4-*b*]pyrazine, and benzobisthiadiazole were retained. In the final Sonogashira reactions, the stable alkynated A_2B_2- and A_3B-porphyrin cores were combined with the brominated acceptors in a mixture of dry toluene and triethylamine under N_2 atmosphere to which $Pd(PPh_3)_2Cl_2$ and CuI were added (Scheme S5 and S6). Typically, three reaction products were obtained, i.e. the desired A-D-A (D-A-D) compound, the expected homocoupled product A-D-D-A (D-A-A-D), and the debrominated acceptor molecule. In all cases, the desired A-D-A (D-A-D) material was the main product. Purification was performed via flash column chromatography followed by preparative (recycling) gel permeation chromatography to yield the six final *meso*-ethynyl-extended porphyrin products shown in Figure 1. Structural characterization of the novel materials was done by ^{1}H-NMR spectroscopy and MALDI-ToF mass spectrometry. All data can be retrieved from the SI.

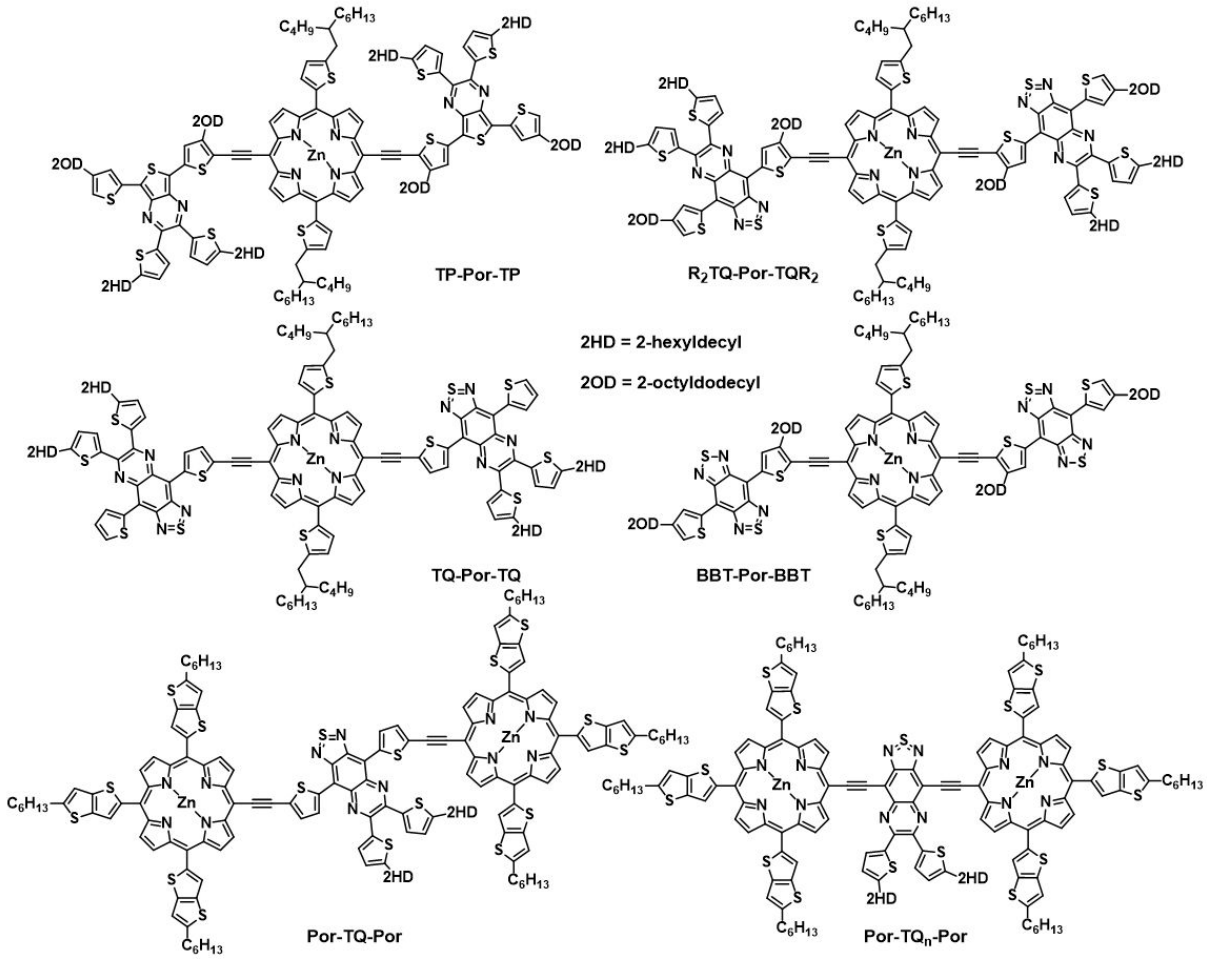

Figure 1: *Chemical structures of the six final meso-ethynyl-extended porphyrin chromophores.*

Analysis of the electrochemical and photophysical properties of the final compounds was performed by cyclic voltammetry (CV) and UV-VIS-NIR absorption spectroscopy (Figure 2 and Table S1). From the UV-VIS-NIR absorption spectra it can be concluded that the acceptor strength – increasing from the TP (**TP-Por-TP**) over the TQ (**R_2TQ-Por-TQR_2 and TQ-Por-TQ**) to the BBT (**BBT-Por-BBT**) variant in case of the A-D-A type porphyrins, and from the 'naked' TQ variant (**Por-TQ$_n$-Por**) to the thiophene-flanked TQ (**Por-TQ-Por**) for the D-A-D type porphyrins – indeed determines the red-shift observed for the intramolecular charge-transfer absorption band at low energy. Peak NIR absorptions (in film) were situated at 786, 919, 929, and 986 nm for **TP-Por-TP**, **R_2TQ-Por-TQR_2**, **TQ-Por-TQ**, and **BBT-Por-BBT**, and 873 and 948 nm for **Por-TQ$_n$-Por** and **Por-TQ-Por**, respectively. Compared to the absorption spectra in solution (Figure S11), an additional red-shift of 130 nm was observed for **TQ-Por-TQ** and assigned to a strong stacking tendency. The π-π stacking behavior was also observed in the MALDI-ToF mass spectrum of the pure material (Figure S6), where two and even three closely interacting molecules bear a single charge. CV measurements (in film, Figure S12) confirmed the increasing acceptor strength trends as the electrochemical bandgap reduced from roughly 1.7 eV for **TP-Por-TP** to 1.5 eV for **R_2TQ-Por-TQR_2**, 1.2 for **TQ-Por-TQ**, and 1.0 eV for **BBT-Por-BBT**, and diminished from 1.3 eV for **Por-TQ$_n$-Por** to 1.2 eV for **Por-TQ-Por** (Table S1).

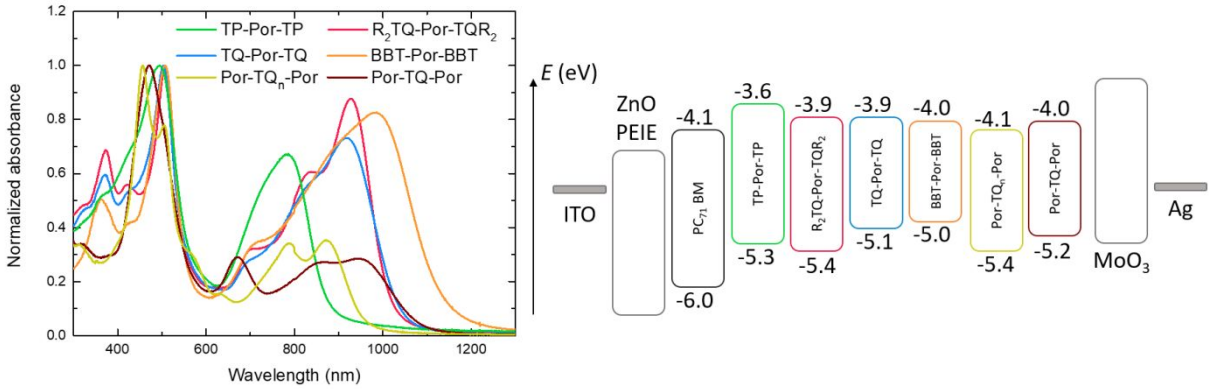

Figure 2: *Absorption spectra of the six neat porphyrin molecules (in film on glass) and energy level diagram displaying the HOMO-LUMO energy levels as derived from CV measurements (Table S1) as well as the different layers used in the inverted OPD device stack.*

Although an optical and electrochemical characterization could be done for the six novel organic semiconductors, only **TQ-Por-TQ** and **Por-TQ-Por** were obtained in a sufficient quantity to allow full optimization in OPD devices. Figure 2 shows the inverted device stack, ITO/ZnO:PEIE/Porphyrin:$PC_{71}BM$/MoO_3/Ag, employed for testing the porphyrin small molecules in OPDs. $PC_{71}BM$ was initially used as the electron acceptor in the bulk heterojunction blends. Device optimization was performed with the aim to enhance the light to dark current density ratio by varying the processing solvent, additives (and their concentration), and spin-coating speed. To further optimize the active layer morphology, solvent vapor annealing (SVA) was applied. Details on the device optimization efforts are discussed in section 2 of the SI. Figure 3a and b show the combined results (*J-V*, EQE, and D^*) of the different optimization steps performed for the **TQ-Por-TQ** and **Por-TQ-Por** based devices, respectively. The specific detectivity was determined using the EQE measured at -2 V and shot noise as the only contribution to the noise current, calculated from the dark currents at -2 V (which is a good approximation according to our previous work [26]). For the **TQ-Por-TQ** devices, deposition from chloroform without additives or SVA yielded the best results, with detectivities up to 4 x 10^{11} Jones in the broad region from 500 to 900 nm (Figure 3a). The use of 1,8-diiodooctane (DIO; 1%) slightly lowered D^* to 2 x 10^{11} Jones but further broadened the spectral range to 1050 nm. Although the addition of pyridine (Pyr; 5%) as a solvent additive increased the open-circuit voltage (V_{OC}) and SVA (40 µL THF for 120 seconds at 40 °C) increased the fill factor (FF) of the photodiodes, both approaches resulted in an overall reduced D^* due to a lower EQE. For **Por-TQ-Por**, deposition from a chlorobenzene solution with 1 v/v% of DIO and Pyr, followed by SVA with CS_2, resulted in a specific detectivity of 4 x 10^{11} Jones in the spectral region from 800 to 1000 nm (Figure 3b). Other optimization trials failed to increase D^*. Preliminary *J-V* results for the **R_2TQ-Por-TQR_2**, **BBT-Por-BBT**, and **Por-TQ_n-Por** blends with $PC_{71}BM$ are shown in Figure S17. For the **R_2TQ-Por-TQR_2** and **BBT-Por-BBT** based devices, overall low light current densities were obtained, while in the case of **Por-TQ_n-Por** a rather high dark current was observed. Additive optimization was performed to a minimal extent, but did not afford significant improvements in device performance.

To further analyze the effects of the device optimization efforts, active layer morphology and response speed studies were conducted. Figure S18 shows the topography of the **TQ-Por-TQ** and **Por-TQ-Por** based blends after processing optimization as obtained by atomic force microscopy (AFM). From these images it can clearly be seen that the optimized blends show an intimate mixing, both for the **TQ-Por-TQ** and **Por-TQ-Por** bulk heterojunctions. For the blends with the **R_2TQ-Por-TQR_2** and **BBT-Por-BBT** donor porphyrins, significant phase separation was observed (Figure S19), explaining the poor charge generation under light conditions. Grazing-incidence wide angle X-ray scattering (GIWAXS) was performed on the optimized blends of **TQ-Por-TQ** and **Por-TQ-Por** to examine the structural differences between the two material systems. In Figure S20 it can be seen that **Por-TQ-Por** exhibits signs of crystalline order, with sharp diffraction peaks which are attributed to the small molecule

phase. Meanwhile, the scattering for the **TQ-Por-TQ** blend is more isotropic with broader scattering peaks, likely due to the presence of an excess of branched side chains which impede ordering in the lamellar direction.

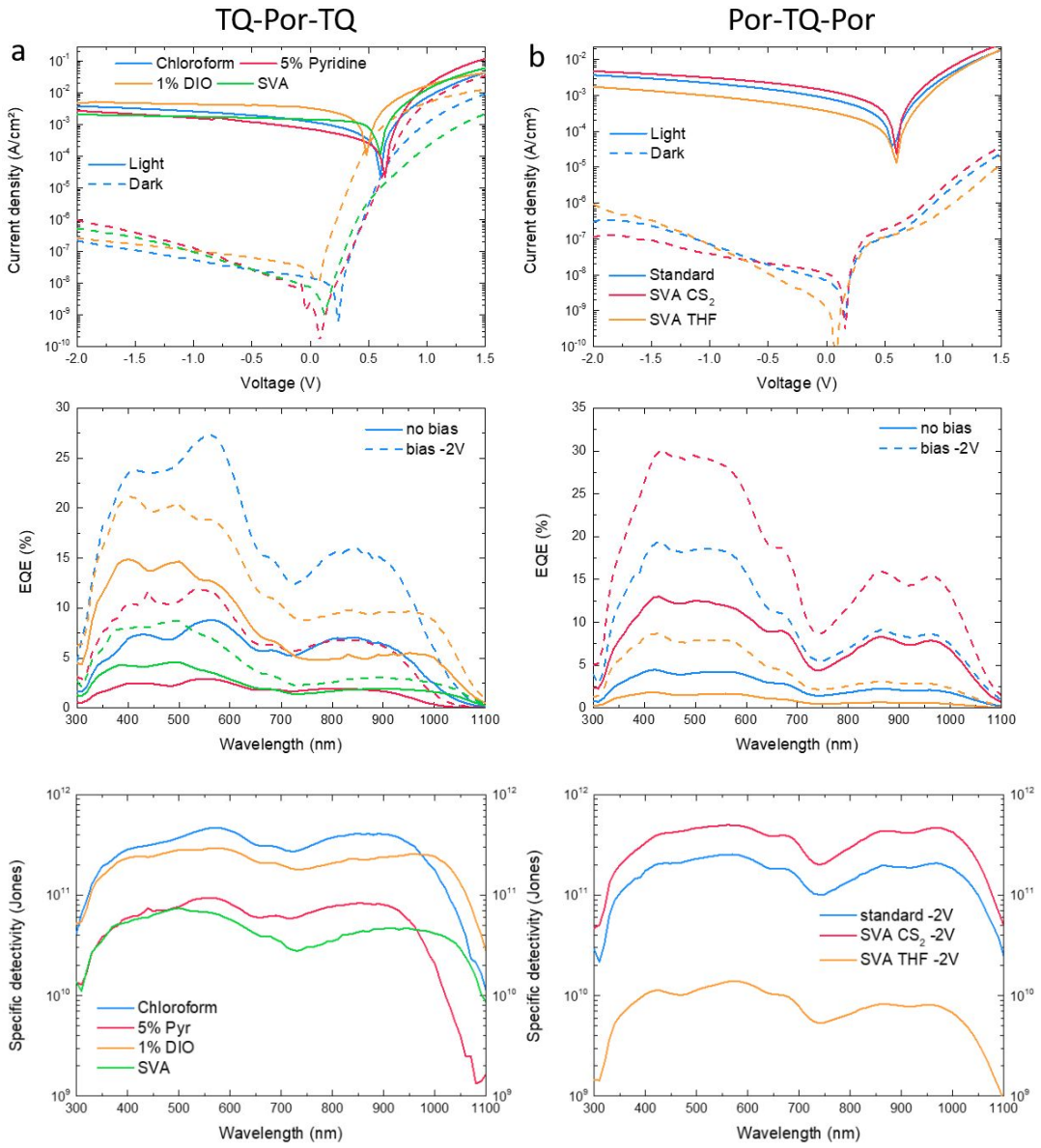

Figure 3: a. *J-V, EQE, and D^* overview for the different optimization efforts performed on the OPD devices prepared with a* ***TQ-Por-TQ****:$PC_{71}BM$ (1:2) active layer blend. Starting with chloroform as the casting solvent, pyridine and DIO were added in 5 and 1 v/v%, respectively, and finally SVA was performed (40 µL THF for 120 seconds at 40 °C).* ***b.*** *J-V, EQE, and D^* overview for the different optimization efforts performed on the OPD devices prepared with a* ***Por-TQ-Por****:$PC_{71}BM$ (1:2) active layer blend. Starting with chlorobenzene as the casting solvent, pyridine and DIO were both added in 1 v/v%, respectively, followed by SVA (40 µL THF or CS_2 for 50 seconds at 40 °C).*

Rise (t_r) and fall (t_f) times were determined for the optimized **TQ-Por-TQ** and **Por-TQ-Por** based OPD devices. The t_r and t_f were calculated from the measurements as depicted in Figure S21. LED light (λ = 450 nm), pulsed with a frequency of 123 Hz, was used to illuminate the devices. The time needed to get the photocurrent signal from 10 to 90% (t_r) corresponds to 435 and 556 µs for the **TQ-Por-TQ** and **Por-TQ-Por** base OPDs, respectively, while the fall times from 90 to 10% (t_f) are 457 and 963 µs, respectively.

In a final experiment, $PC_{71}BM$ was exchanged for 6 different commercially available non-fullerene acceptors (NFAs; structures shown in Figure S22) for the combination with **TQ-Por-TQ**. These NFAs have been shown to significantly increase the performance of bulk heterojunction blends, as shown throughout the OPV field in the past years.[27] An even more interesting property of NFAs, specifically for NIR OPDs, is their capability to be tuned toward NIR absorption. This can boost the EQE in the NIR region and ultimately increase the sensitivity. A general trend we observed for these NFA-containing OPD devices was the low dark current density (J_D), in the order of 10 nA/cm², but unfortunately also low photocurrent density (J_{ph}), below 1 mA/cm² at -2 V bias (under AM1.5G solar illumination, 100 mW cm^{-2}; Figure S23). An exception was the device based on the **TQ-Por-TQ**:Y6 blend, yielding 3 mA/cm² at -2 V bias. Unfortunately, the EQE spectrum suggests that **TQ-Por-TQ** barely contributes to the photocurrent. Figure 4 clearly shows the mismatch of the **TQ-Por-TQ** absorption and the EQE spectrum.[28] A clearly unfavorable blend morphology, as indicated by AFM (Figure S24), is likely at the origin of these poor results.

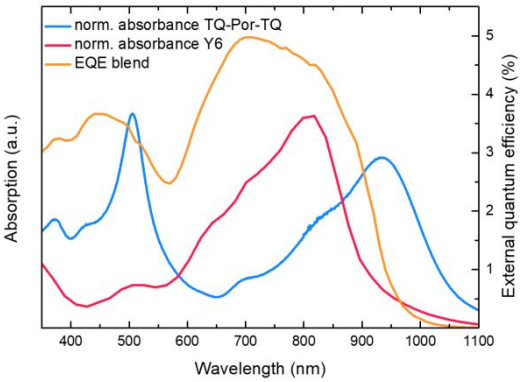

Figure 4: *Overlay of the absorption spectra of neat **TQ-Por-TQ** and Y6 (both in film) and the EQE spectrum of the photodiode prepared from the 1:1 blend.*

Conclusions

Six new *meso*-ethynyl-extended A-D-A and D-A-D-type porphyrin molecules were successfully synthesized. Depending on the acceptor strength, NIR-sensitive small molecules were obtained with a maximum absorption onset up to 1200 nm. Prototype photodetectors prepared from **TQ-Por-TQ** or **Por-TQ-Por**:$PC_{71}BM$ (1:2) blends were optimized in terms of casting solvent, additive concentration, and solvent vapor annealing. This resulted in peak specific detectivities near 2 x 10^{11} and 4 x 10^{11} Jones at 1000 nm (at -2 V bias) for the **TQ-Por-TQ** and **Por-TQ-Por** based photodiodes, respectively. Additionally, six non-fullerene acceptors were tested in combination with the **TQ-Por-TQ** donor. Unfortunately, these devices yielded poor light currents and consequently poor external quantum efficiencies. However, as this is only the second report on *meso*-ethynyl-extended porphyrins for near-infrared organic photodetectors, there is certainly room for further investigations and improvements. Alternatively, **TQ-Por-TQ** could be used in ternary blends to red-shift the absorption and benefit from a well-performing blend combination for sensitive light detection. As multiple promising examples are shown nowadays in both the organic photodetector and solar cell field,[29-33] future work could be in this direction.

Electronic supplementary information

Additional documentation on the synthesis and characterization of the *meso*-ethynyl-extended porphyrins and their precursors (strategy 1 and 2), as well as on the OPD device fabrication, characterization, and optimization, is available as supplementary information.

Conflicts of interest

There are no conflicts to declare.

Acknowledgements

S.G., S.B., and J.V. acknowledge the Research Foundation – Flanders (FWO Vlaanderen) for their Ph.D. fellowships. J.V. also acknowledges funding by FWO Vlaanderen (V413722N) and a personal grant from the District 1630 of Rotary International, supported by the Rotary foundation, allowing a student researcher visit at Stanford University. T.J.Q. acknowledges support from the National Science Foundation Graduate Research Fellowship Program under grant DGE-1656518. This material is based upon work supported by the U.S. Department of Energy, Office of Science, Office of Workforce Development for Teachers and Scientists, Office of Science Graduate Student Research (SCGSR) program. The SCGSR program is administered by the Oak Ridge Institute for Science and Education for the DOE under contract number DE-SC0014664. Use of the Stanford Synchrotron Radiation Light source, SLAC National Accelerator Laboratory, is supported by the U.S. Department of Energy, Office of Science, Office of Basic Energy Sciences under Contract No. DE-AC02-76SF00515. Part of this work was performed at the Stanford Nano Shared Facilities (SNSF), supported by the National Science Foundation under award ECCS-2026822. The authors gratefully acknowledge Prof. Alberto Salleo for his support. K.V. and W.M. are grateful for project funding by the FWO (G0D0118N, G0B2718N, GOH3816NAUHL, and I006320N). Hasselt University and IMOMEC have been partners in the SBO project MIRIS (Monolithic Infrared Image Sensors), supported by VLAIO (Vlaams Agentschap Innoveren en Ondernemen). V.C. thanks the Ministerio de Educación, Cultura y Deporte of Spain for an FPU grant (FPU15/02170). F.L. and P.C. are grateful for project funding by MCI (Spain) (PID2019-105049RB-I00) and MICIU (RED2018-102815-T).

References

1 J. J. Green, J. H. Elisseeff, *Nature*, 2016, **540**, 386.
2 T. Darmanin, F. Guittard, *Materials Today*, 2015, **18**, 273.
3 H. Gernsheim, *A concise history of photography*, Dover Publications, Mineola, New York 1986.
4 G. Wald, *Science*, 1968, **162**, 230.
5 D. Wohrle, *Advanced Materials*, 1997, **9**, 1191.
6 L. Dou, Y. Liu, Z. Hong, G. Li, Y. Yang, *Chemical Reviews*, 2015, **115**, 12633.
7 G. Pirotte, P. Verstappen, D. Vanderzande, W. Maes, *Advanced Electronic Materials*, 2018, **4**, 1700481.
8 K. Vandewal, J. Benduhn, V. C. Nikolis, *Sustainable Energy & Fuels*, 2018, **2**, 538.
9 J. Qi, W. Qiao, Z. Y. Wang, *The Chemical Record*, 2016, **16**, 1531.
10 D. F. Perepichka, M. R. Bryce, C. Pearson, M. C. Petty, E. J. L. McInnes, J. P. Zhao, *Angewandte Chemie International Edition*, 2003, **42**, 4636.
11 Q. Li, Y. Guo, Y. Liu, *Chemistry of Materials*, 2019, **31**, 6359.
12 M. Young, J. Suddard-Bangsund, T. J. Patrick, N. Pajares, C. J. Traverse, M. C. Barr, S. Y. Lunt, R. R. Lunt, *Advanced Optical Materials*, 2016, **4**, 1028.
13 Z. Su, F. Hou, X. Wang, Y. Gao, F. Jin, G. Zhang, Y. Li, L. Zhang, B. Chu, W. Li, *ACS Applied Materials & Interfaces*, 2015, **7**, 2529.
14 J. D. Zimmerman, V. V. Diev, K. Hanson, R. R. Lunt, E. K. Yu, M. E. Thompson, S. R. Forrest, *Advanced Materials*, 2010, **22**, 2780.
15 X. Liu, Y. Lin, Y. Liao, J. Wu, Y. Zheng, *Journal of Materials Chemistry C*, 2018, **6**, 3499.
16 J. Liu, M. Gao, J. Kim, Z. Zhou, D. S. Chung, H. Yin, L. Ye, *Materials Today*, 2021.
17 J. Vanderspikken, W. Maes, K. Vandewal, *Advanced Functional Materials*, 2021, **31**, 2104060.
18 J. Kesters, P. Verstappen, M. Kelchtermans, L. Lutsen, D. Vanderzande, W. Maes, *Advanced Energy Materials*, 2015, **5**, 1500218.
19 V. Piradi, F. Yan, X. Zhu, W.-Y. Wong, *Materials Chemistry Frontiers*, 2021, **5**, 7119.
20 L. Xiao, S. Chen, X. Chen, X. Peng, Y. Cao, X. Zhu, *Journal of Materials Chemistry C*, 2018, **6**, 3341.
21 S. Chen, L. Yan, L. Xiao, K. Gao, W. Tang, C. Wang, C. Zhu, X. Wang, F. Liu, X. Peng, W. Wong, X. Zhu, *Journal of Materials Chemistry A*, 2017, **5**, 25460.
22 L. Li, Y. Huang, J. Peng, Y. Cao, X. Peng, *Journal of Materials Chemistry C*, 2014, **2**, 1372.
23 K. Gao, J. Miao, L. Xiao, W. Deng, Y. Kan, T. Liang, C. Wang, F. Huang, J. Peng, Y. Cao, F. Liu, T. P. Russell, H. Wu, X. Peng, *Advanced Materials*, 2016, **28**, 4727.

24 V. Cuesta, R. Singhal, P. de la Cruz, G. D. Sharma, F. Langa, *ACS Applied Materials & Interfaces*, 2019, **11**, 7216.

25 M. Kelchtermans, J. Deckers, J. Brebels, J. Kesters, P. Verstappen, R. T. Eachambadi, Z. Liu, N. Van den Brande, J. Manca, L. Lutsen, D. Vanderzande, W. Maes, *Organic Electronics*, 2019, **69**, 48.

26 S. Gielen, C. Kaiser, F. Verstraeten, J. Kublitski, J. Benduhn, D. Spoltore, P. Verstappen, W. Maes, P. Meredith, A. Armin, K. Vandewal, *Advanced Materials*, 2020, **32**, 2003818.

27 A. Armin, W. Li, O. J. Sandberg, Z. Xiao, L. Ding, J. Nelson, D. Neher, K. Vandewal, S. Shoaee, T. Wang, H. Ade, T. Heumüller, C. Brabec, P. Meredith, *Advanced Energy Materials,* 2021, **11**, 2003570.

28 J. Yuan, Y. Zhang, L. Zhou, G. Zhang, H.-L. Yip, T.-K. Lau, X. Lu, C. Zhu, H. Peng, P. A. Johnson, M. Leclerc, Y. Cao, J. Ulanski, Y. Li, Y. Zou, *Joule*, 2019, **3**, 1140.

29 H. Li, K. Lu, Z. Wei, *Advanced Energy Materials*, 2017, **7**, 1602540.

30 W. Li, Y. Xu, X. Meng, Z. Xiao, R. Li, L. Jiang, L. Cui, M. Zheng, C. Liu, L. Ding, Q. Lin, *Advanced Functional Materials*, 2019, **29**, 1808948.

31 M. Vartanian, P. de la Cruz, S. Biswas, G. D. Sharma, F. Langa, *Nanoscale*, 2018, **10**, 12100.

32 V. Piradi, X. Xu, Z. Wang, J. Ali, Q. Peng, F. Liu, X. Zhu, *ACS Applied Materials & Interfaces,* 2019, **11**, 6283.

33 L. Nian, Y. Kan, K. Gao, M. Zhang, N. Li, G. Zhou, S. B. Jo, X. Shi, F. Lin, Q. Rong, F. Liu, G. Zhou, A. K. Y. Jen, *Joule*, 2020, **4**, 2223.